A multispeed Discrete Boltzmann Model for transcritical 2D shallow water flows

Michele La Rocca[a], Andrea Montessori[b], Pietro Prestininzi[b], Sauro Succi[c]

[a]*Dipartimento di Ingegneria, Universita' degli Studi Roma TRE, Via Vito Volterra 62, 00146 Rome, Italy,michele.larocca@uniroma3.it,Phone:00390657333453*

[b]*Dipartimento di Ingegneria, Universita' degli Studi Roma TRE, Via Vito Volterra 62, 00146 Rome, Italy*

[c]*Istituto per le Applicazioni del Calcolo, CNR, Via dei Taurini 19, 00189, Rome, Italy*

Abstract

In this work a Discrete Boltzmann Model for the solution of transcritical 2D shallow water flows is presented and validated. In order to provide the model with transcritical capabilities, a particular multispeed velocity set has been employed for the discretization of the Boltzmann equation. It is shown that this particular set naturally yields a simple and closed procedure to determine higher order equilibrium distribution functions needed to simulate transcritical flow. The model is validated through several classical benchmarks and is proven to correctly and accurately simulate both 1D and 2D transitions between the two flow regimes.

Keywords: Shallow water equations, Multispeed Discrete Boltzmann Model, Transcritical flows

1. Introduction

In the last two decades, the Lattice Boltzmann Method has known a growing popularity for the simulation of a variety of complex flows [3, 2]. In particular it has been recognized that some Lattice Boltzmann models can be deduced by discretising the continuous Boltzmann equation over a velocity space of finite dimension and by defining the Equilibrium Distribution Function (EDF) as a Taylor series expansion of the Maxwellian EDF with respect to the flow velocity [13]. The most commonly employed lattices (e.g. 2DQ9 and 3DQ19) guarantee the equivalence of the lattice Boltzmann model with the Navier-Stokes equation only in the low Mach number limit.

This is due to the fact that the velocity sets connected to such lattices are able to exactly reproduce only the lower order hydrodynamic moments of the Maxwellian EDF. In order to correctly reproduce higher order hydrodynamic moments, more complex discrete EDFs are needed which, in turn, require higher dimension velocity spaces [14]. In other words, the highest order of the exactly reproduced hydrodynamic moment is related to the truncation order of the Taylor series expansion of the Maxwellian EDF, which has to be supported by a suitable discretization of the velocity space [20]. A similar limitation is shared by the commonly employed 2DQ9 Lattice Boltzmann models equivalent to Shallow Water Equations [22]. These models, as for the Navier-Stokes equivalent Lattice Boltzmann models, are derived in the limit of low Froude number, the hydraulic counterpart of the Mach number. It is worth recalling that the Froude number is defined as $Fr = U/\sqrt{gh}$, where U is the characteristic depth-averaged flow velocity, h the water depth, and g the gravitational acceleration. As far as Navier-Stokes equation is concerned, the restriction to low Mach number flows still leaves room for the simulation of a number of technically and theoretically interesting flows. On the contrary, in the shallow water framework, the corresponding limitation on the Froude number is a serious shortcoming for real-world applications, where transcritical flows (i.e. flows for which Fr is greater than one) are commonly encountered. A recent work [4] has shown that a 1D transcritical shallow water Lattice Boltzmann model can be constructed by means of asymmetrical lattices. However the extension to 2D is somehow cumbersome. Another way to achieve a Boltzmann-based supercritical model consists in directly integrating in time and space the continuous (in the velocity space) Boltzmann equation, attaining the so-called Gas Kinetic scheme. This approach has been proposed and validated [6, 9, 21, 7], but the intrinsic and intriguing simplicity of the lattice Boltzmann model is lost. The aim of this work is to present and validate a generic multispeed 2D shallow water Discrete Boltzmann Model (DBM), which partially recovers the original simplicity of the Lattice Boltzmann Model, while being able to simulate trans- and supercritical shallow water flows. Hereinafter, by "multispeed", we mean 2D velocity sets with more than 9 elements. An ideal discretization of the velocity space should be such to allow for an arbitrary number of velocities, comply with the isotropy requirements and preserve exactness of the streaming phase, i.e. generate a space filling lattice. The fact that most multispeed discretizations yield non space filling lattices [14] is the main shortcoming of such multispeed velocity sets, because the original simplicity of the Lattice Boltzmann method, intrinsically connected to the streaming phase, is lost. In this work this shortcoming is overcome by employing a conventional finite difference scheme for the solution of the resulting multispeed 2D shallow water DBM. The structure of the paper is as follows: first, the Shallow Water Equations are briefly recalled for the reader's convenience; second, the derivation of a generic multispeed DBM is shown; third, the ability of the proposed DBM is tested by means of some selected benchmark cases; fourth, results are discussed and conclusions are drawn.

2. Shallow Water Equations

The 2D Shallow Water Equations set is:

$$\frac{\partial \mathbf{U}}{\partial t} + \nabla \cdot \underline{\mathbf{E}} = \mathbf{S} \tag{1}$$

where:

$$\mathbf{U} = \begin{pmatrix} h \\ uh \\ vh \end{pmatrix} \underline{\mathbf{E}} = \begin{pmatrix} hu & hv \\ hu^2 + gh^2/2 & huv \\ huv & hv^2 + gh^2/2 \end{pmatrix} \mathbf{S} = \begin{pmatrix} 0 \\ S_x \\ S_y \end{pmatrix} \tag{2}$$

and h, u, v are respectively the water depth and depth-averaged velocity components along horizontal directions x and y. In the above, S_x and S_y are the components of the external force per unit mass along x and y, usually encompassing various effects (bed slope, bed friction, wind-induced surface stress, etc.). The symbol $\nabla\cdot$ stands for divergence operator. The homogeneous part of (1) can be obtained from the the 3D, free surface formulation of the Euler equations, in the limit of "long waves", that is, the perturbations of the free surface having a length much larger than the undisturbed depth [10].

3. Systematic derivation of multispeed EDFs

3.1. Derivation based on Gauss-Hermite quadratures

Consider the following shallow water Maxwellian EDF:

$$f(h, \mathbf{u}, \mathbf{c}) = \frac{1}{\pi g} e^{-\frac{(\mathbf{c}-\mathbf{u}) \cdot (\mathbf{c}-\mathbf{u})}{c_h^2}} \tag{3}$$

where $\mathbf{c} = (c_x, c_y)$ is the particle velocity, $c_h = \sqrt{gh}$ and $\mathbf{u} = (u, v)$. The $(n+m)^{th}$ hydrodynamic moment I_{nm} $(n = 0, 1 \ldots ; m = 0, 1, \ldots)$ is defined as the statistical moment of (3):

$$I_{nm} = \iint_{-\infty}^{+\infty} f\left(h, \mathbf{u}, \mathbf{c}\right) c_x^n c_y^m dc_x dc_y \tag{4}$$

I_{nm} is a generic tensor, whose order is $n + m$. Zero, first and second order hydrodynamic moments $I_{00}, \{I_{10}, I_{01}\}, \{\{I_{20}, I_{11}\}, \{I_{11}, I_{02}\}\}$ are a scalar, a vector and a second order tensor respectively, namely the water depth, the specific discharge and the momentum flux:

$$\begin{gathered} I_{00} = h \\ I_{10} = hu \\ I_{01} = hv \\ I_{20} = \tfrac{gh^2}{2} + hu^2 \\ I_{11} = huv \\ I_{02} = \tfrac{gh^2}{2} + hv^2 \end{gathered} \tag{5}$$

Assuming a finite number of particle velocities (hereinafter referred to as velocity set), a set of EDFs is introduced, which can be approximated by an expansion of the Maxwellian EDF (3) in flow velocity.

The usual 2DQ9 lattice and the EDFs used for shallow water flows are able to correctly reproduce only the hydrodynamic moments (5) and, consequently, flows with $Fr < 1$ [22].

The systematic derivation of velocity sets and the corresponding EDFs able to reproduce high order hydrodynamic moments is based on the Taylor series expansion of (3), with respect to u, v:

$$\begin{aligned} f\left(h, \mathbf{u}, \mathbf{c}\right) \approx \tfrac{1}{\pi g} e^{-\frac{c_x^2}{c_h^2}} \left(1 + 2\tfrac{c_x u}{c_h^2} - \tfrac{u^2}{c_h^2} + 2\left(\tfrac{c_x u}{c_h^2}\right)^2 + \tfrac{4}{3}\left(\tfrac{c_x u}{c_h^2}\right)^3 - 2\tfrac{u^3 c_x}{\left(c_h^2\right)^2} + \ldots\right) \cdot \\ e^{-\frac{c_y^2}{c_h^2}} \left(1 + 2\tfrac{c_y v}{c_h^2} - \tfrac{v^2}{c_h^2} + 2\left(\tfrac{c_y v}{c_h^2}\right)^2 + \tfrac{4}{3}\left(\tfrac{c_y v}{c_h^2}\right)^3 - 2\tfrac{v^3 c_y}{\left(c_h^2\right)^2} + \ldots\right) \end{aligned} \tag{6}$$

The adoption of a $n + m$ truncation order in (6) is a necessary condition to exactly reproduce moments up to the $n+m$ order. If the scaling $\xi = \frac{c_x}{c_h}, \eta = \frac{c_y}{c_h}$ is introduced into (6), the expression of the hydrodynamic moment (4) can be factorised as follows:

$$I_{nm} = h\frac{c_h^{n+m}}{\pi} \left(\int_{-\infty}^{+\infty} \xi^n p\left(\xi\right) e^{-\xi^2} d\xi\right) \left(\int_{-\infty}^{+\infty} \eta^m q\left(\eta\right) e^{-\eta^2} d\eta\right) \tag{7}$$

p, q are real valued functions defined by:

$$\begin{aligned} p\left(\xi\right) = 1 + 2\tfrac{\xi u}{c_h} - \tfrac{u^2}{c_h^2} + 2\left(\tfrac{\xi u}{c_h}\right)^2 + \tfrac{4}{3}\left(\tfrac{\xi u}{c_h}\right)^3 - 2\tfrac{u^3 \xi}{c_h^3} + \ldots \\ q\left(\eta\right) = 1 + 2\tfrac{\eta v}{c_h} - \tfrac{v^2}{c_h^2} + 2\left(\tfrac{\eta v}{c_h}\right)^2 + \tfrac{4}{3}\left(\tfrac{\eta v}{c_h}\right)^3 - 2\tfrac{v^3 \eta}{c_h^3} + \ldots \end{aligned} \tag{8}$$

Integrals in (7) can be approximated by the Gauss-Hermite formula [1]:

$$I_{nm} \approx h c_h^{n+m} \frac{N!M!}{N^2 M^2} \sum_{i=1}^{N} \sum_{j=1}^{M} \frac{2^{N+M-2} (\xi_i)^n (\eta_j)^m p\left(\xi_i\right) q\left(\eta_j\right)}{\left(H_{N-1}\left(\xi_i\right) H_{M-1}\left(\eta_j\right)\right)^2} \tag{9}$$

being H_N, H_M the N^{th}, M^{th} order Hermite polynomials and ξ_i and η_j the i^{th}, j^{th} root of the N^{th}, M^{th} order Hermite polynomials respectively. From (9) it is straightforward to obtain the definitions of the velocity vectors and of the corresponding EDFs. Indeed, define the integer k as $k = ij$. The Cartesian components of the k^{th} velocity vector are obtained as:

$$\mathbf{c}_k = c_h \left\{\xi_i, \eta_j\right\} \quad 1 \leq i \leq N, \quad 1 \leq j \leq M, \quad 1 \leq k \leq NM \tag{10}$$

As a consequence, (9) takes the form:

$$I_{nm} \approx \; h \sum_{k=0}^{N \times M} c_{xk}^n c_{yk}^m \, w_k f_k^e \tag{11}$$

where the k^{th} EDF is given by:

$$f_k^e = p\left(\xi_i\right) q\left(\eta_j\right) \tag{12}$$

and the k^{th} weight coefficient, relative to the k^{th} EDF, by:

$$w_k = c_h^{n+m} \frac{N!M!}{\left(NM\right)^2} \frac{2^{N+M-2}}{\left(H_{N-1}\left(\xi_i\right) H_{M-1}\left(\eta_j\right)\right)^2} \tag{13}$$

It is interesting to observe that, for any given N and M, the following properties hold for the weights and the velocity vectors (10):

$$\begin{aligned} \textstyle\sum_{k=0}^{N \times M} w_k &= 1 \\ \textstyle\sum_{k=0}^{N \times M} w_k c_{xk} = \sum_{k=0}^{N \times M} w_k c_{yk} &= 0 \\ \textstyle\sum_{k=0}^{N \times M} w_k c_{xk}^2 = \sum_{k=0}^{N \times M} w_k c_{yk}^2 &= \tfrac{c_h^2}{2} \\ \textstyle\sum_{k=0}^{N \times M} w_k c_{xk} c_{yk} &= 0 \end{aligned} \tag{14}$$

The third formula in (14) gives the "sound" velocity c_s associated to the chosen velocity set: $c_s^2 = c_h^2/2$ as in in Zhou [22]. Equation (10) allows for the definition of an arbitrary number of velocity sets and of the corresponding EDFs. As stated above, not all such multispeed sets generate Cartesian lattices. But this is not the major shortcoming. Indeed, such a systematic procedure for the definition of sets with an arbitrary number of velocities cannot be adopted in the shallow water framework because the velocity components in (10) depend on the water depth h and thus are not constant. This implies that the set of the Boltzmann-Bhatnagar Gross and Krook (BGK) kinetic equations:

$$\frac{\partial f_k}{\partial t} + \mathbf{c}_k \cdot \nabla f_k = \frac{f_k^e - f_k}{\tau} \quad (1 \leq k \leq N \times M) \tag{15}$$

in force of (10) is not equivalent to the homogeneus part of the Shallow Water Equations (1), being $\mathbf{c}_k$ dependent on h and thus on space and time. In other words, in close analogy with thermal flows, a space-time dependent sound-speed rules out the use of standard equilibria obtainable by the above Gauss-Hermite quadrature, despite the fact that high order hydrodynamic moments can be exactly recovered by using (11).

3.2. Derivation based on the matching of hydrodynamic moments

A velocity set with $N_T + 1$ elements and the corresponding set of EDFs, to be used in the shallow water framework, can be defined starting from a polynomial expression of the k^{th} EDF [20]. In the present work, such polynomial expression retains terms up to fourth order:

$$\begin{aligned} f_k^e = h \Bigg(& A_k + B_k \frac{\mathbf{u}\cdot\mathbf{c}_k}{c_h^2} + C_k \frac{\mathbf{u}\cdot\mathbf{u}}{c_h^2} + D_k \left(\frac{\mathbf{u}\cdot\mathbf{c}_k}{c_h^2}\right)^2 + E_k \left(\frac{\mathbf{u}\cdot\mathbf{c}_k}{c_h^2}\right)^3 + \\ & F_k \frac{(\mathbf{u}\cdot\mathbf{u})(\mathbf{u}\cdot\mathbf{c}_k)}{\left(c_h^2\right)^2} + G_k \left(\frac{\mathbf{u}\cdot\mathbf{u}}{c_h^2}\right)^2 + H_k \frac{(\mathbf{u}\cdot\mathbf{u})(\mathbf{u}\cdot\mathbf{c}_k)^2}{\left(c_h^2\right)^3} + I_k \left(\frac{\mathbf{u}\cdot\mathbf{c}_k}{c_h^2}\right)^4 \Bigg) \end{aligned} \tag{16}$$

The unknown constants $A_k, \ldots, I_k$ have to be determined by matching the discrete hydrodynamic moments of the EDFs (16) with the exact expressions (4):

$$\sum_{k=0}^{N_T} \widetilde{c}_{xk}^m \widetilde{c}_{yk}^n f_k^e = \frac{1}{\pi g} \iint_{-\infty}^{+\infty} c_x^m c_y^n e^{-\frac{(\mathbf{c}-\mathbf{u})\cdot(\mathbf{c}-\mathbf{u})}{c_h^2}} dc_x dc_y \tag{17}$$

where $\widetilde{c}_{xk}, \widetilde{c}_{yk}$ are the Cartesian components of the k^{th} velocity $\widetilde{\mathbf{c}}_k$, $k = 0, \ldots, N_T$. It is necessary to obtain a number of matching conditions from

(17) equal to the number of unknown coefficients. Depending on the choice of the velocity set, the problem can be underdetermined. However, it is possible to reduce the number of constants by exploiting the isotropy properties of the velocity sets [20]. Indeed, velocities having the same magnitude share the same set of constants $A_k, \ldots, I_k$. For this reason, it is useful to group them into subsets, hereinafter referred to as shells, based on their magnitude. In the following we will assume two shells of velocity vectors and the vanishing velocity:

$$\widetilde{\mathbf{c}}_k \equiv \begin{cases} \{0,0\}\,, & k=0 \\ a\,c_0 \left\{\cos\left(\frac{4\pi}{N_T}k\right), \sin\left(\frac{4\pi}{N_T}k\right)\right\}, & 1 \le k \le \dfrac{N_T}{2} \\ b\,c_0 \left\{\cos\left(\frac{4\pi}{N_T}k\right), \sin\left(\frac{4\pi}{N_T}k\right)\right\}, & \dfrac{N_T}{2} < k \le N_T \end{cases} \tag{18}$$

being a, b the dimensionless velocity magnitudes of the two shells, scaled by the constant velocity c_0. In Fig. B.1 an example with $N_T = 16$, is shown.

[Figure 1 about here.]

The number of constants appearing in the definition of the EDFs (16) depends only on the number of shells and on the highest order of terms appearing in (16). Generally speaking, if n_s is the number of shells, the definition of EDFs in (16) need $3 + 9n_s$ constants. In appendix Appendix A the expressions of the 21 constants relative to the two velocity shells (18) are reported: these expressions, obtained imposing matching conditions (17), are valid for any given a, b, c_0, N_T. It is worth noting that coefficients A_k satisfy the same properties (14) of coefficients w_k:

$$\begin{aligned} \textstyle\sum_{k=0}^{N_T} A_k &= 1 \\ \textstyle\sum_{k=0}^{N_T} A_k \widetilde{c}_{xk} = \sum_{k=0}^{N_T} A_k \widetilde{c}_{yk} &= 0 \\ \textstyle\sum_{k=0}^{N_T} A_k \widetilde{c}_{xk}^2 = \sum_{k=0}^{N_T} A_k \widetilde{c}_{yk}^2 &= \tfrac{c_h^2}{2} \\ \textstyle\sum_{k=0}^{N_T} A_k \widetilde{c}_{xk} \widetilde{c}_{yk} &= 0 \end{aligned} \tag{19}$$

4. External forces

External forces of various types can be introduced as source terms in (15) by means of the following expression:

$$\phi_k = 2\frac{\mathbf{F} \cdot \widetilde{\mathbf{c}}_k}{\sum_{j=0}^{N_T} \left(\widetilde{\mathbf{c}}_j \cdot \widetilde{\mathbf{c}}_j\right)} \tag{20}$$

being $\mathbf{F}$ the vector of the external forces. This study only deals with the force induced by the bed slope, whose expression is:

$$\mathbf{F} = -gh\nabla z_b \tag{21}$$

where $z_b = z_b\left(x, y\right)$ is the bottom elevation. Cartesian components F_x, F_y of the external force are obtained as:

$$\begin{array}{l} F_x = \sum_{k=0}^{N_T} \phi_k \widetilde{c}_{xk} \\ F_y = \sum_{k=0}^{N_T} \phi_k \widetilde{c}_{yk} \end{array} \tag{22}$$

Then the kinetic equations (15) with external forces take the form:

$$\frac{\partial f_k}{\partial t} + \widetilde{\mathbf{c}}_k \cdot \nabla f_k = \frac{f_k^e - f_k}{\tau} + \phi_k \quad k = 0, \ldots, N_T \tag{23}$$

The most important property of the multispeed set (18) and the corresponding set of EDFs (16) is the ability of exactly reproducing the hydrodynamic moments up to fourth order. This property, when employed in a Chapman-Enskog expansion of the kinetic equations (23) [15], allows to prove that the kinetic equations (23) are equivalent to the Shallow Water Equations, with an approximation error proportional to ϵ^3, being ϵ the smallness parameter of the Chapman-Enskog expansion. The calculations are standard but rather tedious and are briefly reported in appendix Appendix B for the sake of conciseness. The exact representation of higher order hydrodynamic moments is crucial in providing the model with the ability of simulating transcritical flows, in close analogy with the case of high Mach number flows [14].

5. Results

The $N_T + 1$ kinetic equations (23) are solved by means of a conventional finite difference numerical algorithm on a structured staggered 2D uniform Cartesian grid, employing an explicit first order discretization of the time derivative and a first order upwind discretization of the space derivative [8]. Equilibrium boundary conditions are employed as in Ubertini et al. [19]. Stability is ensured by keeping the Courant number $U_{max}\Delta t/\Delta$ lower than 1, being U_{max} the highest flow velocity in the domain and $\Delta = \Delta x = \Delta y$ the grid spacing. In addition to the abovementioned stability condition on Courant number, the underlying Boltzmann dynamics requires the usual condition on the relaxation time τ^* ($\tau^* = \frac{\tau}{\Delta t} > \frac{1}{2}$) to be fullfilled [17]. It has been previously shown that stable Lattice Boltzmann-based shallow water simulations require high values for the relaxation time, and the resulting viscosity can restrict the field of applicability of such models [12]. For the cases considered here the minimum value for the relaxation time ensuring stability always resulted to be lower than one. In order to assess the ability of the multispeed DBM defined by the EDFs (16), the velocity set (18) and the kinetic equations (23) in simulating transcritical and supercritical shallow water flows, the following benchmark cases have been considered: 1) the one-dimensional (1D) dam-break over a flat surface, 2) the 1D steady flow over an uneven bottom profile and 3) the 2D dam break over a horizontal bed.

5.1. 1D dam-break

The 1D dam break over a flat bottom is a very simple and yet effective case in assessing accuracy and reliability of any numerical method for the shallow water equations. It deals with the transient evolution of an initial discontinuity of the water level around the position $x = 0$. At $t = 0$ the water level h is equal to h_m, for $x \leq 0$, and to h_v, for $x > 0$. This Riemann problem admits the analytical solution of Stoker [16]:

$$h = \begin{cases} h_m, \\ \frac{1}{9g}\left(2\sqrt{gh_m} - \frac{x}{t}\right)^2, \\ h^*, \\ h_v, \end{cases} \qquad u = \begin{cases} u_m, & x < t\sqrt{gh_m} \\ \frac{2}{3}\left(\sqrt{gh_m} + \frac{x}{t}\right), & t\sqrt{gh_m} \leq x < (u^* - c^*)\,t \\ u^*, & (u^* - c^*)\,t \leq x < st \\ u_v & st \leq x \end{cases} \tag{24}$$

where s is the shock's propagation speed, which is a function of the intermediate water depth and velocity, h^*, u^* according to the following relations:

$$\begin{cases} u^* = s - gh_v \frac{1+\sqrt{1+\frac{8s^2}{gh_v}}}{4s} \\ h^* = -\frac{s}{u^*-s} h_v \\ u^* + 2\sqrt{gh^*} = 2\sqrt{gh_m} \end{cases} \tag{25}$$

The typical shape of the Stoker's solution for the 1D dam-break flow is shown in Fig. B.2, where it is compared to the DBM results in terms of depth, flow velocity and Froude number. Numerical results are normalized by h_m (water depth), $\sqrt{gh_m}$ (flow velocity) and L (channel's length).

[Figure 2 about here.]

The agreement is considerably good and it has been quantified by the mean absolute error, whose definition for a generic variable q is:

$$Err\,[q] = \frac{\int |q_{ref}(x) - q(x)| dx}{\int q_{ref}(x) dx} \tag{26}$$

For the case considered $Err[h] \sim 10^{-2}$. The agreement between numerical and analytical flow velocity is as good as for the water depth, the corresponding error $Err[u]$ having the same order of magnitude. The comparison in terms of Froude number shows a discrepancy between numerical and analytical results near the shock which heavily influences the value of a lumped error measure such as (26). The overall agreement is anyway remarkable. It is worth observing the ability of the proposed DBM to smoothly simulate the sub-supercritical transition, without any instability issue, in a case for which the maximum Froude number is equal to: $Fr = 5.74$. The simulation, though intrinsically 1D, has been performed in a 2D domain discretized by 1000×5 nodes. Free-slip boundary conditions are imposed everywhere.

Three different velocity sets have been implemented, obtained by increasing the number of allowed velocities: 21, 41, 81.It is worth noting that, no significant improvement of numerical results has been observed by increasing the number of allowed velocities, as long as it is higher than a minimum value, below which the simulation becomes unstable. Hence, unless otherwise specified, a 21 velocity set model has been used for all the simulations.

It is worth noting that instabilities are generated only if a critical transition ($Fr = 1$) occurs. The spatial resolution affects the accuracy of the front position, i.e. the lower the height h_v the finer the grid needs to be for an accurate representation of the front position, as usual for the numerical solution of shallow water models. Values of the parameters a, b, c_0 have been set to $1, 2, \sqrt{gh_m}$ respectively. The minimum value of the relaxation time ensuring stability was 0.8.

5.2. 1D steady flow over a bottom profile

In this benchmark the ability of simulating a transcritical flow induced by external forces is tested. More specifically, a steady state solution with a known analytical formulation is considered. Consider a 1D straight channel of length L, described by the x abscissa, and having the following bed elevation profile:

$$z_b(x) = \alpha e^{-\left(\frac{x-x_1}{\sigma}\right)^2} + \beta e^{-\left(\frac{x-x_2}{\sigma}\right)^2} + \gamma e^{-\left(\frac{x-x_3}{\sigma}\right)^2} \tag{27}$$

which consists of three consecutive Gaussian bumps, whose crests are respectively located at x_1, x_2, x_3, with elevations α, β, γ, and common variance σ. Fixing the specific (per unit width) discharge q_0 over the whole domain, the critical depth can be calculated as:

$$h_c = \left(\frac{q_0}{\sqrt{g}}\right)^{\frac{2}{3}} \tag{28}$$

Imposing that the current goes through critical depth over the top of the second and third bump (i.e. at $x = x_2, x = x_3$), it is possible, under the hypothesis of no energy dissipation, to analitically derive the steady water depth profile shown in Fig. B.3. This steady motion consists of a subcritical-subcritical flow over the first bump at $x = x_1$, followed by two subcritical-supercritical transitions over the second and third bump at $x = x_2$, $x = x_3$ respectively. Dowstream of the first sub-supercritical transition a super-subcritical transition, i.e. a hydraulic jump, occurs. The hydraulic jump occurs where the upstream supercritical specific thrust equals the downstream subcritical one, that is where: $F(h_u, q_0) = F(h_d, q_0)$, the thrust being defined as:

$$F(h, q_0) = \rho\left(gh^3 + 2q_0^2\right)/2h \tag{29}$$

h_u, h_d, ρ are the water depths upstream and downstream of the hydraulic jump and the density of water respectively. The steady state DBM numerical profile is obtained evolving from an initial uniform water depth, keeping the upstream water depth and discharge fixed. The numerical solution is considered to be steady when the normalized maximum increment I_s between two consecutive timesteps n and $(n-1)$:

$$I_s = \max_i \frac{\left|h_i^n - h_i^{n-1}\right|}{h_i^{n-1}} \tag{30}$$

satisfies the condition: $I_s < 10^{-8}$. The steady state is reached at $t \sim 100s$. In the upper panel of Fig. B.3 the nondimensional analytical and numerical water depth profiles are shown. The water depth scale is the critical depth (28). In the lower panel of Fig. B.3 the analytical and numerical Froude number profiles are shown. All profiles in Fig. B.3 employ a horizontal length scaling equal to σ. The agreement between numerical and analytical data is remarkably good. For the case considered the error (26) is: $Err[h] \sim 10^{-3}$. The super-subcritical transition occurs as a discontinuity, i.e. as an abrupt elevation, of the water depth. This behavior is reflected in the plot of the Froude number shown in Fig. B.3: immediately downstream the smooth sub-supercritical transition occurring over the second bump at $x = x_2$, the inverse transition is revealed by a sudden decrease of the Froude number, caused by an abrupt increase of the depth and a corresponding decrease of the flow velocity, i.e. a bore or hydraulic jump occurring at $31.3 \leq x/\sigma \leq 31.4$. It is worth noting that the bed profile has been chosen in such a way to make this super-subcritical transition occur at a location where the bed slope, though very small, is not null: the analytical solution for both the depth and the flow velocity profile immediately downstream the hydraulic jump thus consists in a smooth variation toward the downstream horizontal profile. The simulation, though intrinsically 1D, has been performed in a 2D domain discretized by 1000×5 nodes. Free-slip conditions have been imposed on all boundaries. For this test case, the parameters a, b, c_0 have been set to $1, 2, \sqrt{gh_0}$ respectively. A set of 81 velocities has been employed. The relaxation time was chosen as $\tau^* = 0.8$.

[Figure 3 about here.]

It is interesting to observe that the numerical steady flow agrees remarkably well with the analytical solution, which has been obtained in the assumption of no dissipative force acting. This suggests that the main source of numerical viscosity for the model under consideration seems to stem from the first order time discretization, and not from the spatial one, which does have some effects, as the next test will show. This test and the previous one demonstrate how the proposed model is able to flawlessly simulate supercritical shallow water regimes with Froude number much higher than any other Boltzmann-based models so far presented in literature.

5.3. 2D dam-break

The 2D dam break test of Fennema & Chaudhry [5] is here considered. It consists of the propagation of a wave triggered by the instantaneous collapse of a lock separating two parts of the domain, each one with a different initial water level at rest (see the sketch in Fig. B.4 for reference). The square domain has a side of $200m$, is divided into two equal parts by a $10m$ thick wall. The wall has a $75m$ wide breach, extending from $y = 95m$ to $y = 170m$.

[Figure 4 about here.]

The initial water level is equal to h_m on the left of the wall (namely $x \leq 95m$), and to h_v on the right of the wall (namely $x > 95m$). At $t = 0s$ the breach is considered open and a 2D dam break flow is generated. Numerical simulations described in the following are relative to a case with $h_m = 10m, h_v = 0.3m$. Such markedly high difference was chosen to produce transcritical 2D shocks. The simulation is characterized by the propagation of a weak, rounded-shaped shock traveling almost perpendicularly to the dividing wall, meanwhile, a rarefaction wave spreads radially into the left part of the domain with a speed which is almost half of the shock's one ((24) gives a close estimate of such celerities). The shock impacts on the opposite wall and is reflected in the form of a strong, wide and backward travelling hydraulic jump; the accumulation of water along the opposite wall spreads laterally and impinges into both lateral walls creating a complicated system of waves traveling back toward the breach and propagating upwind through the aperture into the still basin.

[Figure 5 about here.]

No analytical solution is available for this benchmark thus in this work a well established and validated numerical model has been considered as reference. The reference numerical model integrates the 2D Shallow Water Equations (1) by means of a Finite Volume, shock capturing scheme over an unstructured triangular mesh [11]. It employs a second order Total Variation Diminishing, Weighted Average Flux method [18]. Such scheme has been developed in order to guarantee correct propagation speed of discontinuous solutions, while maintaining a second order accuracy over smooth ones.

[Figure 6 about here.]

The DBM simulation has been carried out on a 100×100 grid. Values of the parameters a, b, c_0 have been set to $1, 2, \sqrt{gh_m}$ respectively. The employed velocity set retained 81 elements and τ^* was set to 0.8. The finite volume numerical simulation has been carried out on an unstructured mesh of 3574 triangular cells.

The assessment of the accuracy of the present model is carried out comparing the time histories of depth and Froude number (Fig. B.5), and specific discharges q_x, q_y (Fig. B.6) at points P_1, P_2, P_3, P_4 (see Fig. B.4 for points' locations), with the results yielded by the reference model. Specific discharges q_x, q_y are defined as: $q_x = uh, q_y = vh$ and scaled with $q_0 = h_m\sqrt{gh_m}$.

The two models substantially yield the same results, being the shape of the time histories very similar at most of the measuring points. The propagation of steep shocks, observable at P2 for example, is well reproduced both in terms of strength and speed, with a slight advance of the proposed model for what concerns the bore reflected by the front wall. It is worth noting that the flow becomes markedly supercritical, as can be seen by inspecting the Froude number values attained at points P_1 and P_2 in Fig. B.5. The proposed model shows a marked numerical viscosity compared to the reference model, due both to the adopted time-space integration of the governing (23) and to the value of the relaxation time.

[Figure 7 about here.]

The main purpose of this benchmark is, as stated above, to check for the ability of the model to correctly compose multidirectional transcritical shocks: based on the outcome of the comparison, it can be concluded that the model possesses such feature. In addition to such quantitative assessment, a general idea on the ability of the proposed multispeed DBM can be gleaned from Fig. B.7, which shows the distribution of the water surface elevation in the whole domain at $t = 26.9s$. In Fig. B.7 both the horizontal and the vertical lenghtscale are expressed in meters. All the most important flow structures are very similar in both panels, in particular the shape and the position of the curved shock.

6. Conclusions

In this work a Discrete Boltzmann Model able to solve the 2D transcritical Shallow Water Equations has been developed and validated. The model employs an original discretization of the continuous particle velocity space consisting of two sets of velocities grouped on the basis of their magnitude. The particular structure of the chosen velocity set allows to significantly reduce the number of unknown coefficients of a fourth order polynomial expression of the Equilibrium Distribution Functions: the coefficients are obtained by matching discrete hydrodynamics moments up to fourth order with their continuos counterparts. The ability of the model to reproduce high order moments is found to provide transcritical capabilities. The benchmarks carried out allowed for a thorough assessment of the ability of the proposed DBM to correctly converge to the solution of the Shallow Water Equations when 1D or 2D strongly supercritical flow structures develop: flows with Froude number up to $Fr \sim 6$ have been accurately simulated. This study shows that Boltzmann-based methods can be extended to the simulation of trans- and supercritical shallow water flows, frequently found in real-world applications.

Appendix A. Definition of the EDF coefficients.

If we define $\phi = c_0/\sqrt{gh}$, for $k = 0$:

$$A_0 = 1 - (a^2 + b^2 - \frac{2}{\phi^2})/(\phi^2 a^2 b^2) \tag{A.1}$$

$$C_0 = (\frac{4}{\phi^2} - a^2 - b^2)/(a^2 b^2) \tag{A.2}$$

$$G_0 = 1/(a^2 b^2) \tag{A.3}$$

Defining $\beta = 1/[N_T(a^2 - b^2)]$, for $1 \leq k \leq \frac{N_T}{2}$:

$$A_k = \beta \frac{2(2 - \phi^2 b^2)}{a^2 \phi^4} \tag{A.4}$$

$$B_k = \beta \frac{4(2 - \phi^2 b^2)}{a^2 \phi^2} \tag{A.5}$$

$$C_k = -\beta \frac{2(2 - \phi^2 b^2)}{a^2 \phi^2} \tag{A.6}$$

$$D_k = \beta \frac{8(3-\phi^2 b^2)}{a^4 \phi^2} \tag{A.7}$$

$$E_k = \beta \frac{16}{3a^4} \tag{A.8}$$

$$F_k = 0 \tag{A.9}$$

$$G_k = -\beta \frac{1}{a^2} \tag{A.10}$$

$$H_k = 0 \tag{A.11}$$

$$I_k = \beta \frac{8}{a^6} \tag{A.12}$$

For $\frac{N_T}{2} + 1 \leq k \leq N_T$:

$$A_k = \beta \frac{2(a^2\phi^2 - 2)}{b^2 \phi^4} \tag{A.13}$$

$$B_k = \beta \frac{4(a^2\phi^2 - 2)}{b^2 \phi^2} \tag{A.14}$$

$$C_k = -\beta \frac{2(a^2\phi^2 - 2)}{b^2 \phi^2} \tag{A.15}$$

$$D_k = \beta \frac{8(a^2\phi^2 - 3)}{b^4 \phi^2} \tag{A.16}$$

$$E_k = \beta \frac{16(2a^2 - 3b^2)}{3b^6} \tag{A.17}$$

$$F_k = -\beta \frac{8(a^2 - b^2)}{b^4} \tag{A.18}$$

$$G_k = \beta \frac{1}{b^4}(3a^2 - 2b^2) \tag{A.19}$$

$$H_k = -\beta \frac{24(a^2 - b^2)}{b^6} \tag{A.20}$$

$$I_k = \beta \frac{8}{b^8}(3a^2 - 4b^2) \tag{A.21}$$

Appendix B. Chapman-Enskog expansion of the kinetic equations (23)

Consider the scaling:

$$
\begin{array}{c}
\widetilde{t} = \frac{c_0 t}{L} \\
\widetilde{\nabla} = L\nabla \\
\widetilde{\tau} = \frac{\tau}{t_c} \\
\epsilon = \frac{c_0 t_c}{L} \\
\widehat{\mathbf{c}}_k = \frac{\widetilde{\mathbf{c}}_k}{c_0} \\
\widetilde{f}_k = \frac{f_k}{H},\ \widetilde{f}_k^e = \frac{f_k^e}{H}
\end{array}
\tag{B.1}
$$

where H, L, t_c are respectively the macroscopic vertical and horizontal lengthscales and the mesoscopic timescale, i.e. the time interval between two successive collisions. Applying the scaling (B.1) to time and space derivatives in (23) and expanding them in perturbative series with respect to the smallness parameter ϵ, (namely the Knudsen number, provided a convective scaling is assumed), the following expressions can be obtained:

$$
\begin{array}{c}
\widetilde{f}_k = \widetilde{f}_k^e + \epsilon f_k^1 + \epsilon^2 f_k^2 + \epsilon^3 f_k^3 + \epsilon^4 f_k^4 + \dots \\
\frac{\partial}{\partial \widetilde{t}} = \frac{\partial}{\partial t_1} + \epsilon \frac{\partial}{\partial t_2} + \epsilon^2 \frac{\partial}{\partial t_3} + \epsilon^3 \frac{\partial}{\partial t_4} + \dots \\
\widetilde{\nabla} = \nabla_1 + \epsilon \nabla_2 + \epsilon^2 \nabla_3 + \epsilon^3 \nabla_4 + \dots
\end{array}
\tag{B.2}
$$

The following equations are obtained at each order:

$$
\begin{array}{c}
\epsilon^0)\ \frac{\partial \widetilde{f}_k^e}{\partial t_1} + \nabla_1 \cdot \left(\widehat{\mathbf{c}}_k \widetilde{f}_k^e\right) = -\frac{f_k^1}{\widetilde{\tau}} \\
\epsilon^1)\ \frac{\partial f_k^1}{\partial t_1} + \nabla_1 \cdot (\widehat{\mathbf{c}}_k f_k^1) + \left(\frac{\partial \widetilde{f}_k^e}{\partial t_2} + \nabla_2 \cdot \left(\widehat{\mathbf{c}}_k \widetilde{f}_k^e\right)\right) = -\frac{f_k^2}{\widetilde{\tau}} \\
\epsilon^2)\ \frac{\partial f_k^2}{\partial t_1} + \nabla_1 \cdot (\widehat{\mathbf{c}}_k f_k^2) + \left(\frac{\partial f_k^1}{\partial t_2} + \nabla_2 \cdot (\widehat{\mathbf{c}}_k f_k^1)\right) + \left(\frac{\partial \widetilde{f}_k^e}{\partial t_3} + \nabla_3 \cdot \left(\widehat{\mathbf{c}}_k \widetilde{f}_k^e\right)\right) = -\frac{f_k^3}{\widetilde{\tau}} \\
\epsilon^3)\ \frac{\partial f_k^3}{\partial t_1} + \nabla_1 \cdot (\widehat{\mathbf{c}}_k f_k^3) + \left(\frac{\partial f_k^2}{\partial t_2} + \nabla_2 \cdot (\widehat{\mathbf{c}}_k f_k^2)\right) + \left(\frac{\partial f_k^1}{\partial t_3} + \nabla_3 \cdot (\widehat{\mathbf{c}}_k f_k^1)\right) + \left(\frac{\partial \widetilde{f}_k^e}{\partial t_4} + \nabla_4 \cdot \left(\widehat{\mathbf{c}}_k \widetilde{f}_k^e\right)\right) = -\frac{f_k^4}{\widetilde{\tau}} \\
\vdots
\end{array}
\tag{B.3}
$$

Summing (B.3) with respect to k and accounting for the fact that:

$$
\begin{array}{c}
\sum_{k=0}^{N_T} \widetilde{f}_k^e = \frac{h}{H} \\
\sum_{k=0}^{N_T} \widehat{\mathbf{c}}_k \widetilde{f}_k^e = \frac{h\mathbf{u}}{c_0 H} \\
\sum_{k=0}^{N_T} f_k^i = 0;\ i = 1, 2, \dots \\
\sum_{k=0}^{N_T} \widehat{\mathbf{c}}_k f_k^i = 0;\ i = 1, 2, \dots
\end{array}
\tag{B.4}
$$

it is straightforward to obtain the shallow water mass balance equation, which in dimensional form is given by:

$$\frac{\partial h}{\partial t} + \nabla\left(h\mathbf{u}\right) = 0 \tag{B.5}$$

Multiplying each (B.3) by $\widehat{\mathbf{c}}_k$, summing with respect to k and accounting for the definitions of the hydrodynamic moments:

$$\begin{gathered}\Im_2 = \sum_{k=0}^{N_T} \widehat{\mathbf{c}}_k \widehat{\mathbf{c}}_k \widetilde{f}_k^e = \frac{1}{c_0^2 H}\left(h\mathbf{u}\otimes\mathbf{u} + g\frac{h^2}{2}\mathbf{I}\right)\\ \Im_3 = \sum_{k=0}^{N_T} \widehat{\mathbf{c}}_k \widehat{\mathbf{c}}_k \widehat{\mathbf{c}}_k \widetilde{f}_k^e\\ \Im_4 = \sum_{k=0}^{N_T} \widehat{\mathbf{c}}_k \widehat{\mathbf{c}}_k \widehat{\mathbf{c}}_k \widehat{\mathbf{c}}_k \widetilde{f}_k^e\end{gathered}$$

where symbol $\otimes$ indicates the dyadic product of the vector $\mathbf{u}$ with itself and $\mathbf{I}$ is the identity matrix, the following form of the macroscopic momentum balance equation is obtained:

$$\begin{gathered}\frac{\partial h\mathbf{u}}{\partial t} + \nabla\cdot\left(h\mathbf{u}\otimes\mathbf{u} + g\frac{h^2}{2}\mathbf{I}\right) = \frac{c_0^2 H}{L}\left[\epsilon\widetilde{\tau}\nabla_1\cdot\left(\frac{\partial\Im_2}{\partial t_1} + \nabla_1\cdot\Im_3\right) + \right.\\ \epsilon^2\widetilde{\tau}\nabla_2\cdot\left(\frac{\partial\Im_2}{\partial t_1} + \nabla_1\cdot\Im_3\right) + \epsilon^2\widetilde{\tau}\nabla_1\cdot\left(\frac{\partial\Im_2}{\partial t_2} + \nabla_2\cdot\Im_3\right) - \\ \left. -\epsilon^2\widetilde{\tau}\nabla_1\cdot\left(\frac{\partial^2\Im_2}{\partial t_1^2} + 2\frac{\partial}{\partial t_1}\nabla_1\cdot\Im_3 + \nabla_1\cdot\nabla_1\cdot\Im_4\right) + \epsilon^3\ldots\right]\end{gathered} \tag{B.6}$$

Thus (23), together with the velocity set (18) and the EDFs (16) are equivalent to the shallow water momentum balance equation (2). The equivalence is meant in the limit of small ϵ. The approximation error is proportional to ϵ^3, due to the fact that the proposed EDFs (16) together with the velocity set (18) are able to reproduce exactly all the hydrodynamic moments appearing at right hand side of (B.6): i.e. the first term which is not correctly reproduced in (B.6) is proportional to ϵ^3. This is the reason of the ability of the proposed discrete Boltzmann equation in simulating trans- and supercritical shallow water flows.

[1] Abramowitz, Milton & Stegun, Irene A 2012 Handbook of mathematical functions: with formulas, graphs, and mathematical tables. Courier Dover Publications.

[2] Aidun, Cyrus K. & Clausen, Jonathan R. 2010 Lattice-Boltzmann Method for Complex Flows. Annual Review of Fluid Mechanics **42** (1), 439–472.

[3] Benzi, R., Succi, S. & Vergassola, M. 1992 The lattice boltzmann equation: theory and applications. Physics Reports **222** (3), 145–197.

[4] Chopard, Bastien, Pham, VT & Lefevre, Laurent 2013 Asymmetric lattice boltzmann model for shallow water flows. Computers & Fluids **88**, 225–231.

[5] Fennema, Robert J & Chaudhry, M Hanif 1990 Explicit methods for 2-d transient free surface flows. Journal of Hydraulic Engineering **116** (8), 1013–1034.

[6] Ghidaoui, MS, Deng, JQ, Gray, WG & Xu, K 2001 A boltzmann based model for open channel flows. International journal for numerical methods in fluids **35** (4), 449–494.

[7] Ghidaoui, MS, Kolyshkin, AA, Liang, JH, Chan, FC, Li, Q & Xu, K 2006 Linear and nonlinear analysis of shallow wakes. Journal of Fluid Mechanics **548**, 309–340.

[8] Hirsch, Charles 2007 Numerical computation of internal and external flows: the fundamentals of computational fluid dynamics, , vol. 1. Butterworth-Heinemann.

[9] Liang, JH, Ghidaoui, MS, Deng, JQ & Gray, WG 2007 A boltzmann-based finite volume algorithm for surface water flows on cells of arbitrary shapes. Journal of Hydraulic Research **45** (2), 147–164.

[10] Mei, Chiang C 1989 The applied dynamics of ocean surface waves, , vol. 1. World scientific.

[11] Prestininzi, Pietro 2009 Numerical modelling of fluvial floods. PhD thesis, Università degli Studi RomaTre.

[12] Prestininzi, Pietro, Sciortino, Giampiero & La Rocca, Michele 2013 On the effect of the intrinsic viscosity in a two-layer shallow water lattice boltzmann model of axisymmetric density currents. Journal of Hydraulic Research **51** (6), 668–680.

[13] Shan, XW & He, XY 1998 Discretization of the velocity space in the solution of the Boltzmann equation. PHYSICAL REVIEW LETTERS **80** (1), 65–68.

[14] Shan, Xiaowen, Yuan, Xue-Feng & Chen, Hudong 2006 Kinetic theory representation of hydrodynamics: a way beyond the navier–stokes equation. Journal of Fluid Mechanics **550**, 413–441.

[15] Sterling, James D & Chen, Shiyi 1996 Stability analysis of lattice boltzmann methods. Journal of Computational Physics **123** (1), 196–206.

[16] Stoker, James Johnston 2011 Water waves: The mathematical theory with applications, , vol. 36. John Wiley & Sons.

[17] Succi, S. 2001 The Lattice Boltzmann equation for fluid dynamics and beyond. Oxford: Oxford Science Publications.

[18] Toro, EF 1989 A weighted average flux method for hyperbolic conservation laws. Proc. R. Soc. Lond. A **423** (1865), 401–418.

[19] Ubertini, S., Bella, G. & Succi, S. 2003 Lattice Boltzmann method on unstructured grids: Further developments. Physical Review E **68** (1), 1–10.

[20] Watari, Minoru & Tsutahara, Michihisa 2004 Possibility of constructing a multispeed bhatnagar-gross-krook thermal model of the lattice boltzmann method. Physical Review E **70** (1), 016703.

[21] Xu, Kun 2002 A well-balanced gas-kinetic scheme for the shallow-water equations with source terms. Journal of Computational Physics **178** (2), 533–562.

[22] Zhou, Jian 2004 Lattice Boltzmann Methods for Shallow Water Flows. Berlin: Springer.

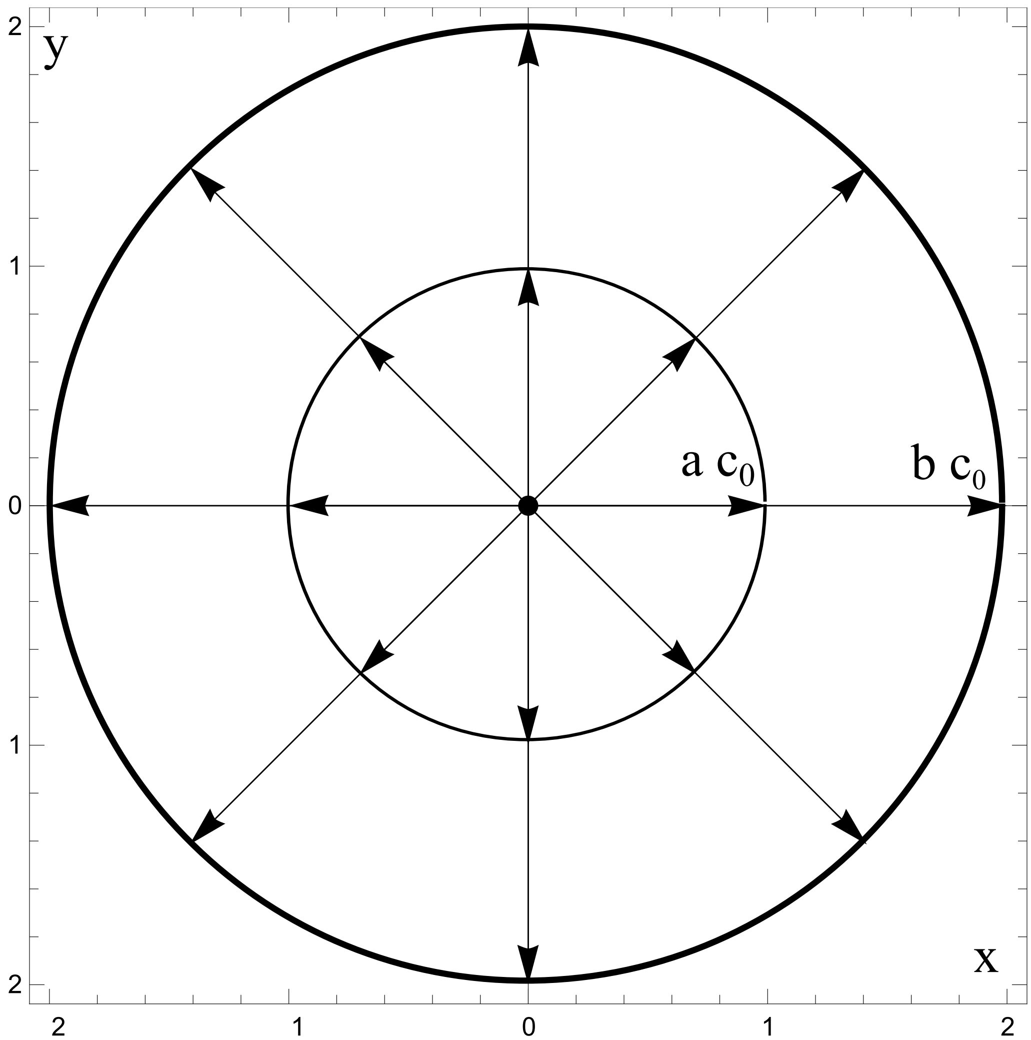

Figure B.1: Sketch of the velocity set

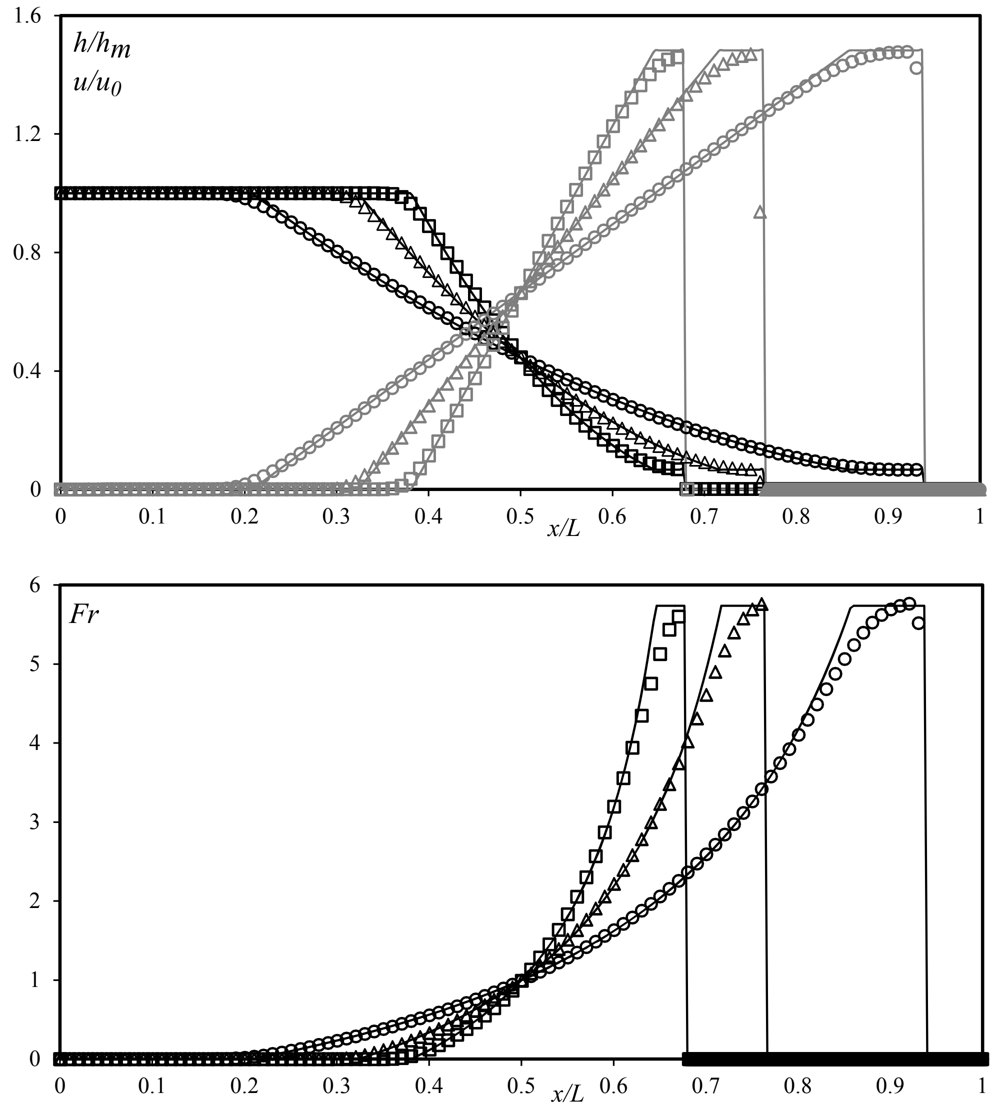

Figure B.2: 1D dam-break, comparison between analytical (solid traces) and numerical results (markers): upper panel, nondimensional water depth (black traces) and fluid velocity profiles (grey traces); lower panel, Froude Number profile. $t^* = 0.12$: $\square$; $t^* = 0.17$: $\triangle$; $t^* = 0.29$: $\bigcirc$; where $t^* = t\sqrt{gh_m}/L$

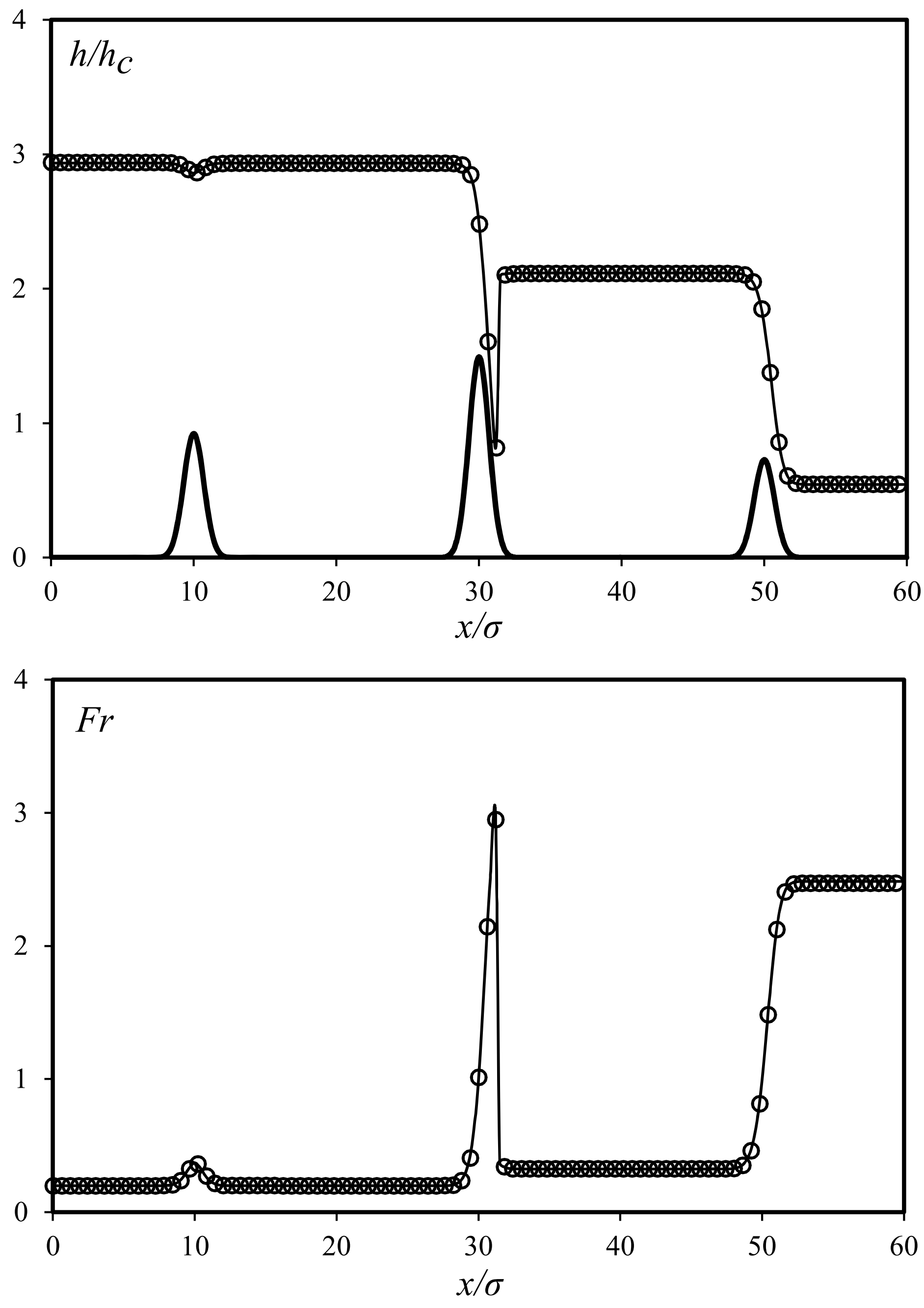

Figure B.3: 1D Steady flow profiles over gaussian bumps, comparison between analytical (solid traces) and numerical (markers) results: upper panel, nondimensional water depth; lower panel, Froude number.

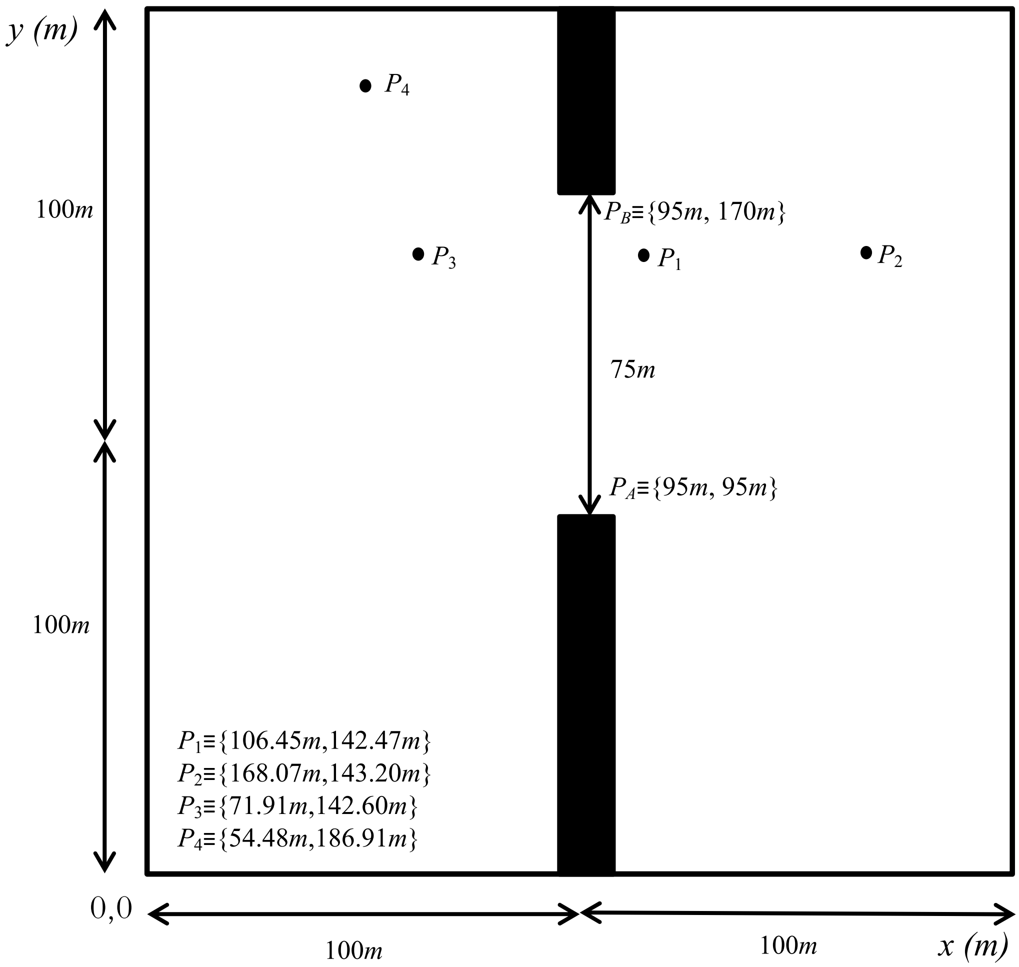

Figure B.4: Sketch of the 2D dam break benchmark of Fennema & Chaudhry [5].

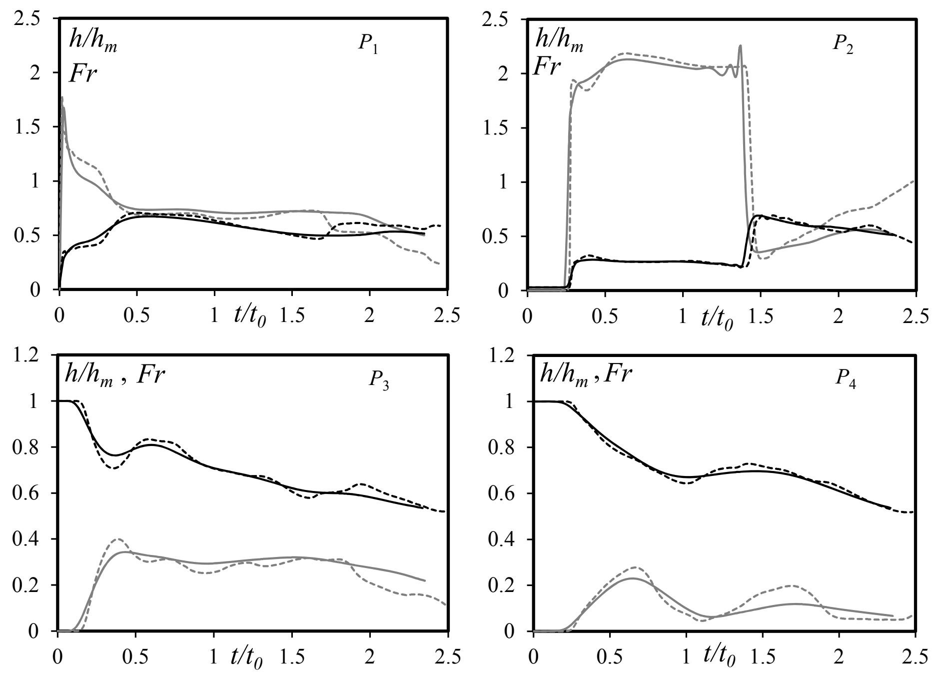

Figure B.5: Time histories of nondimensional water depth (black trace) and Froude number (grey trace) at gauge locations. Comparison between numerical model (solid traces) and reference solution (dashed traces).

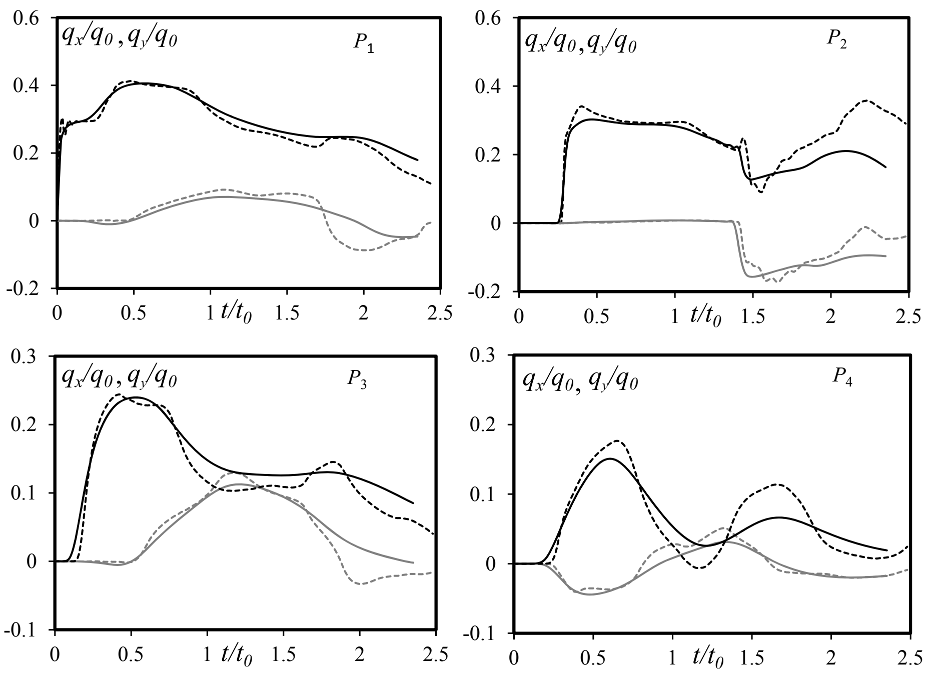

Figure B.6: Time histories of nondimensional specific discharge (along x-direction black traces, along y-direction, grey traces) at gauge locations. Comparison between numerical model (solid traces) and reference solution (dashed traces).

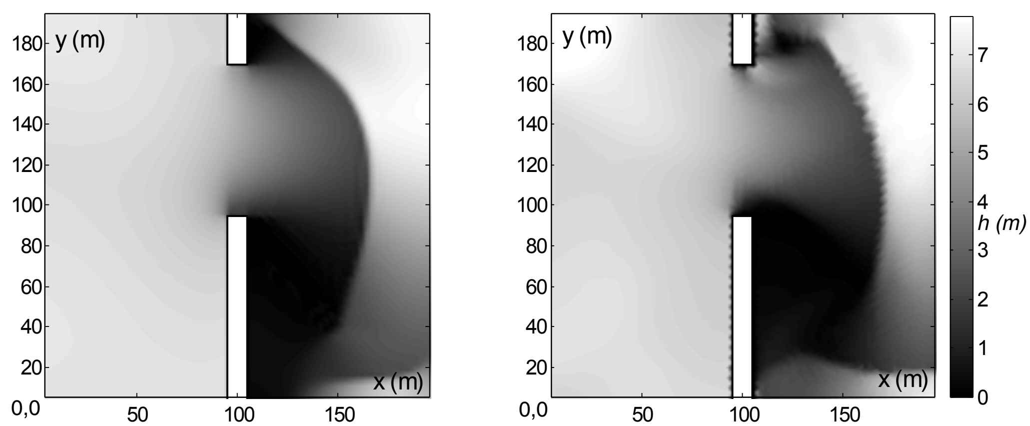

Figure B.7: 2D plot of the water depth in the whole domain at $t = 29s$. Left panel: DBM numerical results. Right panel: numerical reference results. Distances and water depth values are expressed in meters.